crystals

MDPI

*Article*

# Effect of Fluoroalkyl-Substituent in Bistolane-Based Photoluminescent Liquid Crystals on Their Physical Behavior

**Shigeyuki Yamada [1,*], Yizhou Wang [1], Masato Morita [1], Qingzhi Zhang [2], David O'Hagan [2], Masakazu Nagata [3], Tomohiro Agou [3], Hiroki Fukumoto [3], Toshio Kubota [3], Mitsuo Hara [4] and Tsutomu Konno [1]**

[1] Faculty of Molecular Chemistry and Engineering, Kyoto Institute of Technology, Matsugasaki, Sakyo-ku, Kyoto 606-8585, Japan; kit.fusso.201906@gmail.com (Y.W.); kit.fusso.201602@gmail.com (M.M.); konno@kit.ac.jp (T.K.)
[2] School of Chemistry, University of St. Andrews, North Haugh, St. Andrews KY 15 5EA, UK; qz@st-andrews.ac.uk (Q.Z.); do1@st-andrews.ac.uk (D.O.)
[3] Department of Quantum Beam Science, Graduate School of Science and Engineering, Ibaraki University, 4-12-1 Naka-narusawa, Hitachi, Ibaraki 316-8511, Japan; 20nd153x@vc.ibaraki.ac.jp (M.N.); tomohiro.agou.mountain@vc.ibaraki.ac.jp (T.A.); hiroki.fukumoto.chem@vc.ibaraki.ac.jp (H.F.); toshio.kubota.organicchem@vc.ibaraki.ac.jp (T.K.)
[4] Graduate School of Engineering, Nagoya University, Furo-cho, Chikusa-ku, Nagoya 464-8603, Japan; mhara@chembio.nagoya-u.ac.jp
* Correspondence: syamada@kit.ac.jp; Tel.: +81-75-724-7517

**Abstract:** Photoluminescent liquid crystals (PLLCs) have attracted significant attention owing to their broad applicability in thermosensing and PL switching. Extensive efforts have been made to develop bistolane-based PLLCs containing flexible units at both molecular terminals, and it has been revealed that their PL behavior can switch with the phase transition between the crystalline and LC phases. Although slight modulation of the flexible unit structure dramatically alters the LC and PL behaviors, few studies into the modification of the flexible units have been conducted. With the aim of achieving dynamic changes in their physical behaviors, we developed a family of bistolane derivatives containing a simple alkyl or a fluoroalkyl flexible chain and carried out a detailed systematic evaluation of their physical behaviors. Bistolanes containing a simple alkyl chain showed a nematic LC phase, whereas switching the flexible chain in the bistolane to a fluoroalkyl moiety significantly altered the LC phase to generate a smectic phase. The fluoroalkyl-containing bistolanes displayed a stronger deep blue PL than their corresponding non-fluorinated counterparts, even in the crystalline phase, which was attributed to the construction of rigid molecular aggregates through intermolecular F···H and F···F interactions to suppress non-radiative deactivation.

**Keywords:** alkyl; bistolane; fluoroalkyl; flexible chain; liquid crystal; photoluminescence; π-conjugate



**Citation:** Yamada, S.; Wang, Y.; Morita, M.; Zhang, Q.; O'Hagan, D.; Nagata, M.; Agou, T.; Fukumoto, H.; Kubota, T.; Hara, M.; et al. Effect of Fluoroalkyl-Substituent in Bistolane-Based Photoluminescent Liquid Crystals on Their Physical Behavior. *Crystals* **2021**, *11*, 450. https://doi.org/10.3390/cryst11040450

Academic Editor: Mikhail Osipov

Received: 1 April 2021
Accepted: 17 April 2021
Published: 20 April 2021



## 1. Introduction

The fluorine atom possesses numerous unique characteristics [1–4], including the largest electronegativity of all elements (4.0 on the Pauling scale), the second smallest atomic size (van der Waals radius, $r_{vdw}$ = 147 pm) next to hydrogen ($r_{vdw}$ = 120 pm), and the dissociation energy of the C–F bond (105.3 kJ mol$^{-1}$) is higher than those of the C–H (98.8 kJ mol$^{-1}$) and C–C (83.1 kJ mol$^{-1}$) bonds. Owing to these unique characteristics, the incorporation of fluorine atoms into organic molecules results in dramatic augmentations or alterations in their physical properties, in addition to introducing new functionalities [1–4]. Over the past few decades, significant attention has been paid to the development of fluorinated functional materials, worldwide. Consequently, several fluorinated materials have been developed for application in the pharmaceutical [5–7], agrochemical [8–10], and industrial fields, including organic dyes, liquid crystals, and photoluminescence molecules (Figure 1a) [11–13].

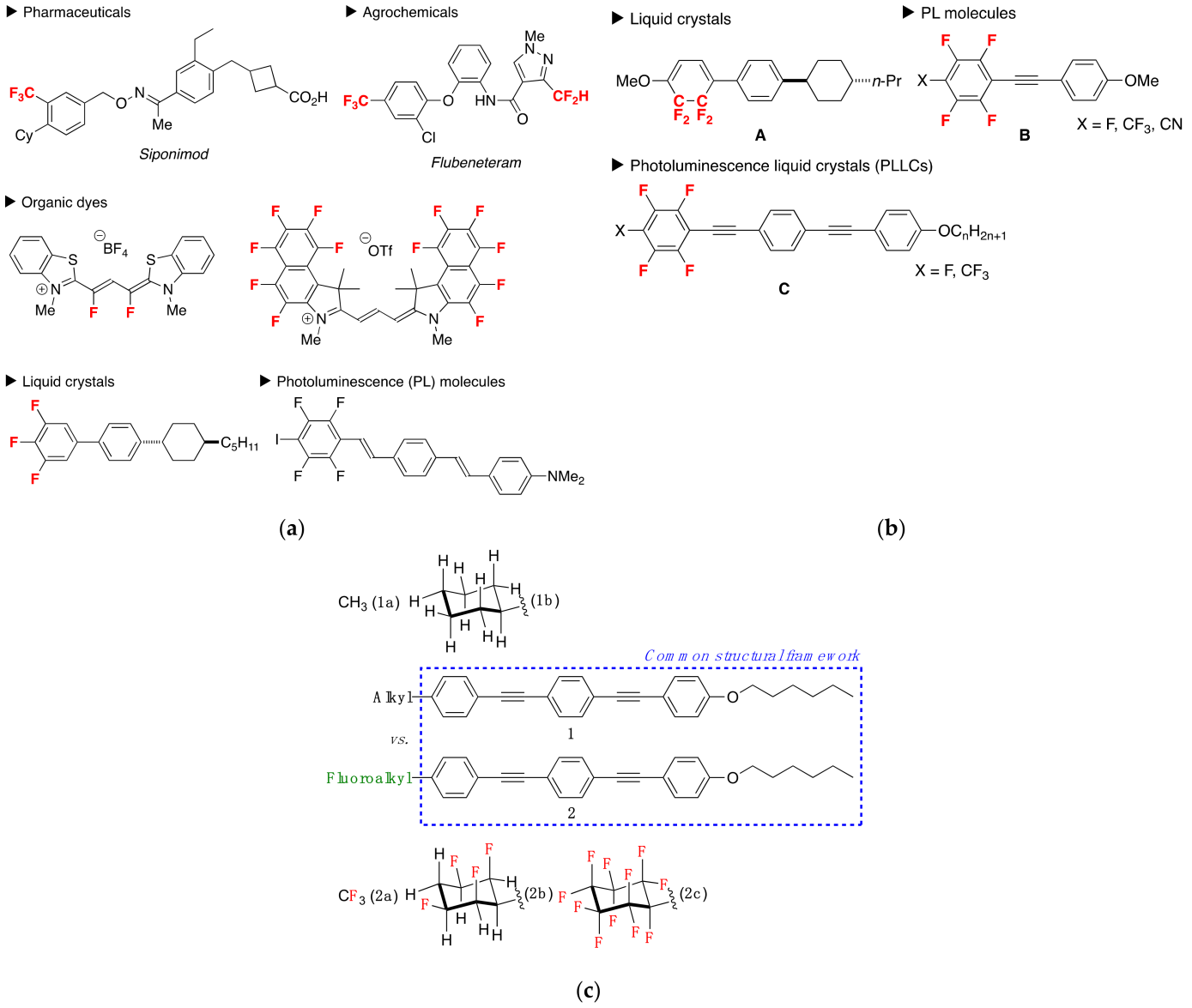


**Figure 1.** (**a**) Examples of fluorine-containing organic materials reported by other groups, and (**b**) by our group; (**c**) chemical structures of bistolanes **1** (bearing an alkyl chain) and **2** (bearing a fluoroalkyl unit).

Previously, our group developed an efficient synthetic methodology for a wide variety of organofluorine compounds using readily available fluorinated substances [14,15] and carried out detailed explorations of fluorine-containing organic materials, such as negative dielectric liquid-crystalline (LC) molecules (**A**) [16] and efficient solid-state photoluminescence (PL) molecules (**B**) (Figure 1b) [17,18]. From the latter studies on fluorinated PL molecules, an interesting finding was that polyfluorinated bistolanes (**C**) exhibited both LC and PL properties [19–23] and were, thus, promising stimulus-responsive PL switching molecules [24,25]. As a result of intensive investigations into fluorinated PL molecules, it was revealed that fluorine atoms in these structures play an essential role in determining the electron density distribution and in the construction of rigid molecular aggregates via F···H hydrogen bonding interactions.

To understand the effect of the fluoroalkyl-type flexible unit on the LC and PL characteristics of bistolane-based photoluminescent LCs (PLLCs) (see Figure 1c), we designed a family of bistolane derivatives **1** bearing an alkyl chain (e.g., methyl or cyclohexyl) and bistolane derivatives **2** bearing a fluoroalkyl unit (e.g., trifluoromethyl, 2,3,5,6-tetrafluorocyclohexyl or undecafluorocyclohexyl). In this article, we discuss the

results of our evaluation of the phase transitions and photophysical behaviors of these derivatives and describe in detail the effects of the fluoroalkyl substituents on the physical properties of the bistolane derivatives.

## 2. Materials and Methods

### *2.1. General*

All chemicals were of reagent grade and were purified in the usual manner prior to use when necessary. Column chromatography was conducted using silica gel (FUJIFILM Wako Pure Chemical Corporation, Wako-gel® 60N, 38–100 μm; Osaka, Japan), while thin-layer chromatography (TLC) was performed on silica gel TLC plates (Merck, Silica gel 60$F_{254}$; New Jersey, NJ, USA).

High-resolution mass spectra (HRMS) were recorded on a JMS700MS spectrometer (JEOL, Tokyo, Japan) using the fast atom bombardment (FAB) method. Infrared (IR) spectra were recorded using the KBr method with an FTIR-4100 type A spectrometer (JASCO, Tokyo, Japan). All the optical spectra are reported in terms of the wavenumber ($cm^{-1}$). $^{1}H$ NMR (400 MHz) and $^{13}C$ NMR (100 MHz) spectra were obtained using an AVANCE III 400 NMR spectrometer (Bruker, Rheinstetten, Germany) in chloroform-*d* ($CDCl_3$) solution, and the chemical shifts are reported in parts per million (ppm) based on the residual protons in the NMR solvent. $^{19}F$ NMR (376 MHz) spectra were obtained using an AVANCE III 400 NMR spectrometer (Bruker, Rheinstetten, Germany) in $CDCl_3$ solution with $CFCl_3$ ($\delta_F$ = 0 ppm) as an internal standard.

### *2.2. Materials*

Bistolanes **1a** and **1b** bearing an alkyl chain and **2a**–**2c** bearing a fluoroalkyl unit were synthesized via a Sonogashira cross-coupling reaction using 4-substituted halobenzene and 4-[2-(4-*n*-hexyloxyphenyl)ethyn-1-yl]phenylacetylene, both of which are readily accessible from the corresponding commercially-available chemicals (Figure 2).

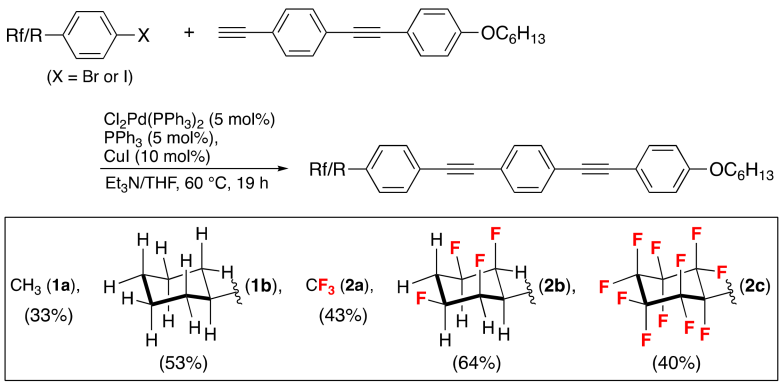


**Figure 2.** Synthetic procedures for the preparation of the bistolanes **1a**, **1b**, and **2a**–**2c** used in this study.

### *2.3. Typical Synthetic Procedure for Preparation of the Bistolanes (as an Example,* **2c***)*

In a two-necked round-bottomed flask, equipped with a magnetic stirrer bar, were placed $Cl_2Pd(PPh_3)_2$ (Sigma-Aldrich; 22 mg, 0.031 mmol), $PPh_3$ (Fujifilm-Wako Pure Chemicals; 10 mg, 0.038 mmol), 4-[2-(4-*n*-hexyloxyphenyl)ethyn-1-yl]phenylacetylene (76 mg, 0.33 mmol), 1-(undecafluorocyclohexyl)-4-iodobenzene (191 mg, 0.39 mmol), CuI (Fujifilm-Wako Pure Chemicals; 6.0 mg, 0.032 mmol), and $Et_3N$ (Fujifilm-Wako Pure Chemicals; 1.5 mL). The mixture was heated to 60 °C and continuously stirred for 19 h at the same temperature. After 19 h, the precipitate formed in the reaction mixture was removed by atmospheric filtration, the filtrate was added to an aqueous saturated $NH_4Cl$ solution (Fujifilm-Wako Pure Chemicals; 10 mL), and the organic component was extracted with ethyl acetate (EtOAc, 3 × 15 mL). The combined organic layer was then dried over anhydrous $Na_2SO_4$ and separated by filtration. The filtrate was evaporated under reduced pressure using a ro-

tary evaporator and the residue was subjected to silica-gel column chromatography (eluent: hexane/EtOAc = 30/1), followed by recrystallization from $CH_2Cl_2$/MeOH ($v/v$ = 1/1) to afford 1-undecafluorocyclohexyl-4-[2-[4-[2-(4-*n*-hexyloxyphenyl)ethyn-1-yl]phenyl]ethyn-1-yl]benzene (**2c**) as colorless crystals in 40% yield (87 mg, 0.13 mmol).

2.3.1. 1-Undecafluorocyclohexyl-4-[2-[4-[2-(4-*n*-hexyloxyphenyl)ethyn-1-yl]phenyl]ethyn-1-yl]benzene (**2c**)

Yield: 40%; m.p.: 163 °C determined by DSC; IR (KBr) $\nu_{max}$ 2960, 2933, 2861, 2213, 1597, 1521, 1249, 1195, 1025, 968, 866 $cm^{-1}$; $^1H$ NMR ($CDCl_3$) $\delta$ 0.91 (3H, t, $J$ = 6.8 Hz), 1.31–1.39 (4H, m), 1.42–1.53 (2H, m), 1.79 (2H, quin., $J$ = 6.4 Hz), 3.98 (2H, t, $J$ = 6.4 Hz), 6.88 (2H, d, $J$ = 8.8 Hz), 7.46 (2H, d, $J$ = 8.8 Hz), 7.51 (3H, s), 7.67 (4H, s); $^{13}C$ NMR ($CDCl_3$) $\delta$ 14.0, 22.6, 25.7, 29.1, 29.7, 31.6, 68.1, 87.6, 89.3, 91.9, 104.2–114.0 (m, 2C), 114.6, 114.7, 121.8, 123.7, 123.9, 124.2, 126.8, 127.0 (t, $J$ = 4.4 Hz), 127.2 (t, $J$ = 3.6 Hz), 131.4, 131.6, 131.9, 133.1, 159.5; $^{19}F$ NMR ($CDCl_3$): $\delta$ −118.4 to −119.5 (dm, $J$ = 295.5 Hz, 2F), −121.9 to −123.0 (dm, $J$ = 275.5 Hz, 2F), −123.0 to −124.1 (dm, $J$ = 286.1 Hz, 1F), −132.7 to −133.8 (dm, $J$ = 298.5 Hz, 2F), −138.4 to −139.6 (dt, $J$ = 282.0, 13.6 Hz, 2F), −141.6 to −142.7 (dm, $J$ = 286.1 Hz, 1F), −181.0 to −181.4 (m, 1F); HRMS (FAB+) $m/z$ 658.1720 (calcd for $C_{34}H_{25}F_{11}O$, 658.1730).

2.3.2. 4-[2-[4-[2-(4-*n*-Hexyloxyphenyl)ethyn-1-yl]phenyl]ethyn-1-yl]toluene (**1a**)

Yield: 33%; m.p.: 154 °C determined by DSC; IR (KBr) $\nu_{max}$ 2952, 2921, 2848, 1604, 1519, 1466, 1284, 1242, 1180, 839, 813 $cm^{-1}$; $^1H$ NMR ($CDCl_3$) $\delta$ 0.91 (3H, t, $J$ = 7.2 Hz), 1.31–1.39 (4H, m), 1.40–1.52 (2H, m), 1.75–1.83 (2H, m), 2.37 (3H, s), 3.97 (2H, t, $J$ = 6.4 Hz), 6.87 (2H, d, $J$ = 8.8 Hz), 7.16 (2H, d, $J$ = 8.4 Hz), 7.42 (2H, d, $J$ = 8.4 Hz), 7.45 (2H, d, $J$ = 8.8 Hz), 7.475 (4H, s); $^{13}C$ NMR ($CDCl_3$) $\delta$ 14.0, 21.5, 22.6, 25.7, 29.2, 31.5, 68.1, 87.8, 88.6, 91.26, 91.34, 114.6, 114.9, 120.0, 122.9, 123.3, 129.1, 131.3, 131.4, 131.5, 133.0, 138.5, 159.4; HRMS (FAB+) $m/z$ 392.2148 (calcd for $C_{29}H_{28}O$, 392.2140).

2.3.3. 1-Cyclohexyl-4-[2-[4-[2-(4-*n*-hexyloxyphenyl)ethyn-1-yl]phenyl]ethyn-1-yl]benzene (**1b**)

Yield: 53%; m.p.: 164 °C determined by DSC; IR (KBr) $\nu_{max}$ 2926, 2852, 2215, 1604, 1596, 1518, 1246, 1103, 827 $cm^{-1}$; $^1H$ NMR ($CDCl_3$) $\delta$ 0.91 (3H, t, $J$ = 7.2 Hz), 1.21–1.30 (1H, m), 1.30–1.52 (10H, m), 1.70–1.92 (8H, m), 3.97 (2H, t, $J$ = 6.4 Hz), 6.87 (2H, d, $J$ = 8.8 Hz), 7.19 (2H, d, $J$ = 8.4 Hz), 7.449 (2H, d, $J$ = 8.4 Hz), 7.454 (2H, d, $J$ = 8.8 Hz), 7.47 (4H, s); $^{13}C$ NMR ($CDCl_3$) $\delta$ 14.0, 22.6, 25.7, 26.1, 26.8, 29.1, 31.5, 34.2, 44.5, 68.1, 87.8, 88.5, 91.3, 114.5, 114.8, 120.3, 122.9, 123.2, 126.9, 129.6, 131.3, 131.4, 131.6, 133.0, 148.6, 159.3; HRMS (FAB+) $m/z$ 460.2760 (calcd for $C_{34}H_{36}O$, 460.2766).

2.3.4. 4-[2-[4-[2-(4-*n*-Hexyloxyphenyl)ethyn-1-yl]phenyl]ethyn-1-yl]benzotrifluoride (**2a**)

Yield: 43%; m.p.: 130 °C determined by DSC; IR (KBr) $\nu_{max}$ 2962, 2937, 2859, 1607, 1594, 1510, 1332, 1286, 1251, 1127, 1067, 1024, 837 $cm^{-1}$; $^1H$ NMR ($CDCl_3$) $\delta$ 0.91 (3H, t, $J$ = 6.8 Hz), 1.32–1.38 (4H, m), 1.40–1.52 (2H, m), 1.73–1.86 (2H, m), 3.98 (2H, t, $J$ = 6.8 Hz), 6.88 (2H, d, $J$ = 8.8 Hz), 7.46 (2H, d, $J$ = 8.8 Hz), 7.50 (4H, s), 7.62 (4H, d, $J$ = 1.6 Hz); $^{13}C$ NMR ($CDCl_3$) $\delta$ 14.0, 22.6, 25.7, 29.2, 31.6, 68.1, 87.6, 89.5, 91.5, 91.9, 114.6, 114.7, 121.2 (q, $J$ = 271.3 Hz), 121.8, 124.2, 125.3 (q, $J$ = 3.7 Hz), 126.9, 130.0 (q, $J$ = 33.0 Hz), 131.4, 131.6, 131.8, 133.1, 159.5; $^{19}F$ NMR ($CDCl_3$): $\delta$ −63.30 (s, 3F); HRMS (FAB+) $m/z$ 446.1861 (calcd for $C_{29}H_{25}F_3O$, 446.1858).

2.3.5. 1-(2,3,5,6-Tetrafluorocyclohexyl)-4-[2-[4-[2-(4-*n*-hexyloxyphenyl)ethyn-1-yl]phenyl]ethyn-1-yl]benzene (**2b**)

Yield: 64%; m.p.: 175 °C determined by DSC; IR (KBr) $\nu_{max}$ 2934, 2868, 2213, 1604, 1519, 1247, 1107, 1016, 973, 837 $cm^{-1}$; $^1H$ NMR ($CDCl_3$) $\delta$ 0.91 (3H, t, $J$ = 6.8 Hz), 1.31–1.39 (4H, m), 1.41–1.52 (2H, m), 1.79 (2H, quin., $J$ = 6.8 Hz), 2.43–2.56 (1H, m), 2.62 (1H, t, $J$ = 36.4 Hz), 2.70–2.86 (1H, m), 3.97 (2H, t, $J$ = 6.4 Hz), 4.51–4.77 (2H, m), 4.87–5.18 (2H, m), 6.87 (2H, d, $J$ = 8.8 Hz), 7.46 (2H, d, $J$ = 8.4 Hz), 7.491 (6H, brs), 7.54 (2H, d, $J$ = 8.4 Hz); $^{13}C$

NMR ($CDCl_3$) $\delta$ 14.0, 22.6, 25.7, 29.1, 31.6, 43.6–44.2 (m, 1C), 68.1, 85.6–90.0 (2C), 87.7, 89.9, 90.4, 114.6, 114.8, 122.4, 123.1, 123.7, 129.3, 131.3, 132.0, 133.1, 135.7, 159.4, three carbons cannot be detected due to low solubility in NMR solvent; $^{19}$F NMR ($CDCl_3$): $\delta$ −190.6 to −190.9 (m, 2F), −210.1 to −210.6 (m, 2F); HRMS (FAB+) *m/z* 532.2402 (calcd for $C_{34}H_{32}F_4O$, 532.2389).

### *2.4. X-ray Crystallographic Analysis*

Single crystals of **2a** and **2c** were obtained by recrystallization from a mixed solvent system of $CH_2Cl_2$/MeOH ($v/v$ = 1/1). Each single crystal was mounted on a glass fiber and X-ray diffraction patterns were recorded on a XtaLabMini diffractometer equipped with a VariMax Mo optical system (λ = 0.71073 Å) and a Pilatus P200 detector (Rigaku, Tokyo, Japan). The reflection data were processed using the CryslAlisPro (ver. 1.171.38.46; Rigaku Oxford Diffraction, 2015). The structures were solved by a directed method (SHELXT-2014/5) and SHELXL-2014/7 programs [26]. The crystallographic data were deposited in the Cambridge Crystallographic Data Centre (CCDC) database (CCDC 2,065,068 for **2a** and 2,065,069 for **2c**). These data can be obtained free of charge from the CCDC via www.ccdc.cam.ac.uk/data_request/cif (accessed on 19 April 2021).

### *2.5. Powder X-ray Diffraction (PXRD) Measurements*

The liquid crystal structures were evaluated using an FR-E X-ray diffractometer attached to an R-axis IV two-dimensional (2D) detector (Rigaku, Tokyo, Japan). For the purpose of these measurements, 0.3-mm collimated Cu *Kα* radiation (λ = 1.54187 Å) was used as the X-ray beam, and the camera length was set to 300 mm. The powder sample was loaded into a thin-walled glass capillary tube for XRD analysis ($\phi$ 1.0–2.5 mm, Hilgenberg GmbH), and the sample was annealed up to an isotropic temperature under vacuum. The glass capillary was placed on a ceramic heater attached to the FR-E sample holder. The exposure time of the X-ray beam was 5–60 min.

### *2.6. Computations*

All computations were performed using the Gaussian 16 software package (*Revision* B.01) [27]. Geometry optimizations were carried out using the hybrid meta-GGA functional (M06-2X) [28,29] and the 6-31+G(d) basis set with an implicit solvation model (conductor-like polarizable continuum model; CPCM [30–32]) for $CH_2Cl_2$. The vertical excitation energies and dipole moments of the optimized structures were calculated using the time-dependent self-consistent field approximation [33,34] at the same level of theory.

### *2.7. Thermal Measurements*

The phase transition behavior was observed by polarizing optical microscopy using a BX53 microscope (Olympus Corporation, Tokyo, Japan), equipped with a heating and cooling stage (Linkam Scientific Instruments, 10,002 L, Surrey, UK). The thermodynamic behavior was determined using differential scanning calorimetry (DSC, SHIMADZU DSC-60 Plus, Kyoto, Japan) at heating and cooling rates of 5.0 °C min$^{-1}$ under a $N_2$ atmosphere.

### *2.8. Photophysical Measurements*

The UV–Vis absorption spectra were recorded using a V-500 absorption spectrometer (JASCO, Tokyo, Japan). The PL spectra of the solution and crystal forms were acquired using an FP-6600 fluorescence spectrometer (JASCO, Tokyo, Japan). The absolute quantum yields in both the solution and crystalline phases were measured using the Quantaurus-QY measurement system C11347-01 (Hamamatsu Photonics, Hamamatsu, Japan).

## 3. Results and Discussion

### *3.1. Theoretical Assessment*

Our study was initiated with a theoretical assessment based on quantum chemical calculations using the Gaussian 16 software to discuss the effects of the fluoroalkyl units

on the physical properties of the various compounds. Table 1 lists the molecular dipole moments (i.e., $\mu_{||}$ along the major molecular axis and $\mu_{\perp}$ along the minor molecular axis), the highest occupied molecular orbital (HOMO) and lowest unoccupied MO (LUMO) energies, the theoretical transition probability and distribution, and the theoretical absorption wavelength ($\lambda^{calcd}$) for each compound. Figure 3 illustrates the MOs alongside the corresponding orbital energies.

**Table 1.** Theoretical data obtained from quantum chemical calculations [1].

| Compound | $\mu_{\|\|}/\mu_{\perp}$ (D) [2] | HOMO/LUMO (eV) | Theoretical Transition Probability (%) | $\lambda^{calcd}$ (nm) |
|---|---|---|---|---|
| **1a** | 0.96/1.79 | −6.88/−1.27 | HOMO→LUMO (92%) | 330 |
| **1b** | 0.96/1.79 | −6.87/−1.27 | HOMO→LUMO (92%) | 331 |
| **2a** | 6.19/1.49 | −6.99/−1.50 | HOMO→LUMO (87%) | 333 |
| **2b** | 2.44/4.17 | −6.93/−1.35 | HOMO→LUMO (91%) | 331 |
| **2c** | 6.57/1.54 | −7.00/−1.52 | HOMO→LUMO (87%) | 334 |

[1] The ground state geometry and the TD-SCF approximation were obtained at the M06-2X/6-31+G(d) level of theory with CPCM for $CH_2Cl_2$. [2] $\mu_{||}$ and $\mu_{\perp}$ are the dipole moments along the major and minor molecular axes, respectively.

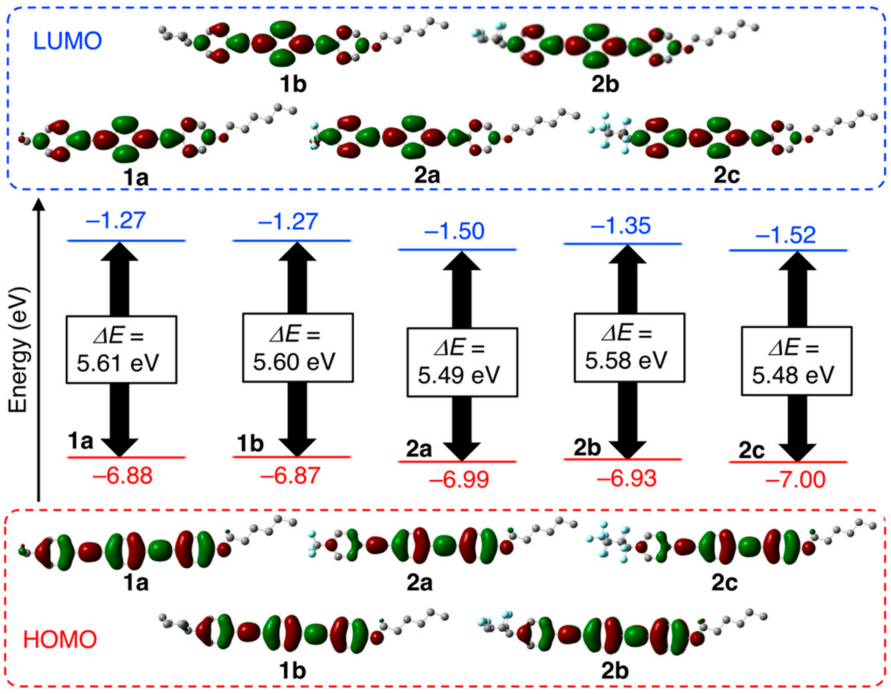


**Figure 3.** Molecular orbitals and orbital energies for bistolanes **1a** and **1b** (bearing an alkyl chain), and **2a**–**2c** (bearing a fluoroalkyl unit). In the MO diagrams, hydrogen atoms are omitted for clarity from the molecular structures.

Bistolanes **1a** and **1b**, bearing an alkyl chain, were found to possess small dipole moments for both the major and minor molecular axes, $\mu_{||}$ and $\mu_{\perp}$, respectively, in both the major and minor molecular axes in the ground state. Comparing the $\mu_{||}$ and $\mu_{\perp}$ values for **1a** and **1b**, the $\mu_{||}$ values for perfluoroalkyl-containing bistolanes **2a** and **2c** increased approximately six-fold along the major molecular axis. Interestingly, in the case of bistolane **2b**, bearing an all-*cis*-2,3,5,6-tetrafluorocyclohexyl unit, ~2.5-fold higher values of both $\mu_{||}$ and $\mu_{\perp}$ were obtained because of the 1,3-diaxial arrangement of the C–F bonds stemming from the all-*cis* configuration [35,36]. The dramatic changes in the dipole moments may, therefore, induce a significant alteration in the molecular aggregates, associated with changes in the intermolecular interactions; a significant change in the phase transition

behavior during the crystal ⇄ LC and LC ⇄ isotropic liquid phase transformations would also be expected.

Based on our calculations, **1a** and **1b**, both of which bear alkyl chains, exhibited broad HOMOs and LUMOs that covered the entire π-conjugated structure. In contrast, the partially or fully fluoroalkyl-containing bistolanes **2a**–**2c** showed a molecular orbital distribution wherein the orbital lobes were primarily localized over the electron-rich aromatic ring attached to the *n*-hexyloxy chain in the HOMO, while in the LUMO, the orbital lobes were primarily localized over the electron-deficient aromatic ring bearing a fluoroalkyl unit. **1a** and **1b** exhibited high energy levels of −6.88 eV and −6.87 eV for the HOMO, respectively, and −1.27 eV for both LUMOs of **1a** and **1b** ($\Delta E$ = 5.60–5.61 eV). Meanwhile, **2a** and **2c** with the perfluoroalkyl substituent exhibited reduced HOMO and LUMO energy levels, i.e., −7.00 eV and −1.52 eV, respectively, together with a smaller $\Delta E$ value (5.48 eV). Notably, **2b**, with a partially fluorinated alkyl fragment, had intermediate HOMO and LUMO energy levels between **1b** and **2c**: −6.93 eV for the HOMO and −1.35 eV for the LUMO. Consequently, it can be anticipated that switching the flexible unit from an alkyl chain to the corresponding fluoroalkyl unit could also result in significant changes in the photophysical behavior, such as the ultraviolet-visible (UV–Vis) absorption and the PL behavior.

### *3.2. Synthesis and Crystal Structure Determination*

Based on the theoretical assessments, bistolanes **1** and **2** were synthesized via a Pd(0)-catalyzed Sonogashira cross-coupling reaction of 4-[2-(4-*n*-hexyloxyphneyl)ethyn-1-yl]phenylacetylene with the appropriate iodobenzene or bromobenzene bearing an alkyl or fluoroalkyl substituent at the *para*-position (Figure 2). All compounds were successfully obtained in 33–64% isolated yields after purification by column chromatography and subsequent recrystallization. Identification of the crystalline compounds was achieved by spectroscopic analyses, and the obtained products were found to be sufficiently pure to allow evaluation of their phase transitions and PL behaviors.

Among the crystalline compounds obtained, trifluoromethyl ($CF_3$)-containing **2a** and undecafluorocyclohexyl (*cyclo*-$C_6F_{11}$)-substituted **2c** furnished single crystals suitable for X-ray crystallographic analysis. Figure 4 shows the molecular structures and packing structures of these two crystals.

As indicated, the $CF_3$-containing **2a** formed colorless rod-shaped single crystals of a monoclinic crystal system in the *Cc* space group, and the unit cell contained four molecular units. For **2a**, a rigid packing structure was constructed that included several intermolecular interactions (Figure 4a, left). Considering the short interatomic distances, as shown in Figure 4a (right), C–F···H hydrogen bonding (259.5 pm), O···H hydrogen bonding (268.4 pm), C–F···π interactions (316.4 pm) [37–39], C–H···π interactions (282.4 and 284.0 pm), and van der Waals interactions ($C_{alkyl}$–H···H–$C_{alkyl}$ = 235.3 pm and $C_{aryl}$–H···H–$C_{alkyl}$ = 237.7 pm) all appeared to be present; in each of these cases, the interatomic distances were less than the sum of $r_{vdW}$, for the two atoms (i.e., C: 170 pm, H: 120 pm, and F: 149 pm) [40]. In contrast, the *cyclo*-$C_6F_{11}$-substituted **2c** formed colorless block-shaped crystals of a monoclinic crystal system in the $P2_1$ space group, and four molecular units of **2c** were contained in a unit cell (Figure 4b, left). As shown in Figure 4b (right), rigid packing structures were formed through several intermolecular interactions, including C–F···H hydrogen bonding (242.8 and 254.7 pm), C–F···F interactions (289.4, 291.1, 293.9, and 294.0 pm) [41,42], $C_{aryl}$–H···π interactions (282.2, 283.0, and 289.4 pm), $C_{alkyl}$–H···π interactions (283.8 pm), and van der Waals interactions ($C_{aryl}$–H···H—$C_{alkyl}$ = 238.8 pm). It is notable that **2a** produced layered structures with a head-to-tail molecular alignment through C–F···H hydrogen bonding interactions. Although **2c** also formed layered structures with a head-to-head molecular alignment, in this case, these were attributed to C–F···F interactions resulting from the fluorophilic effect of the highly fluorinated alkyl moieties [42,43].

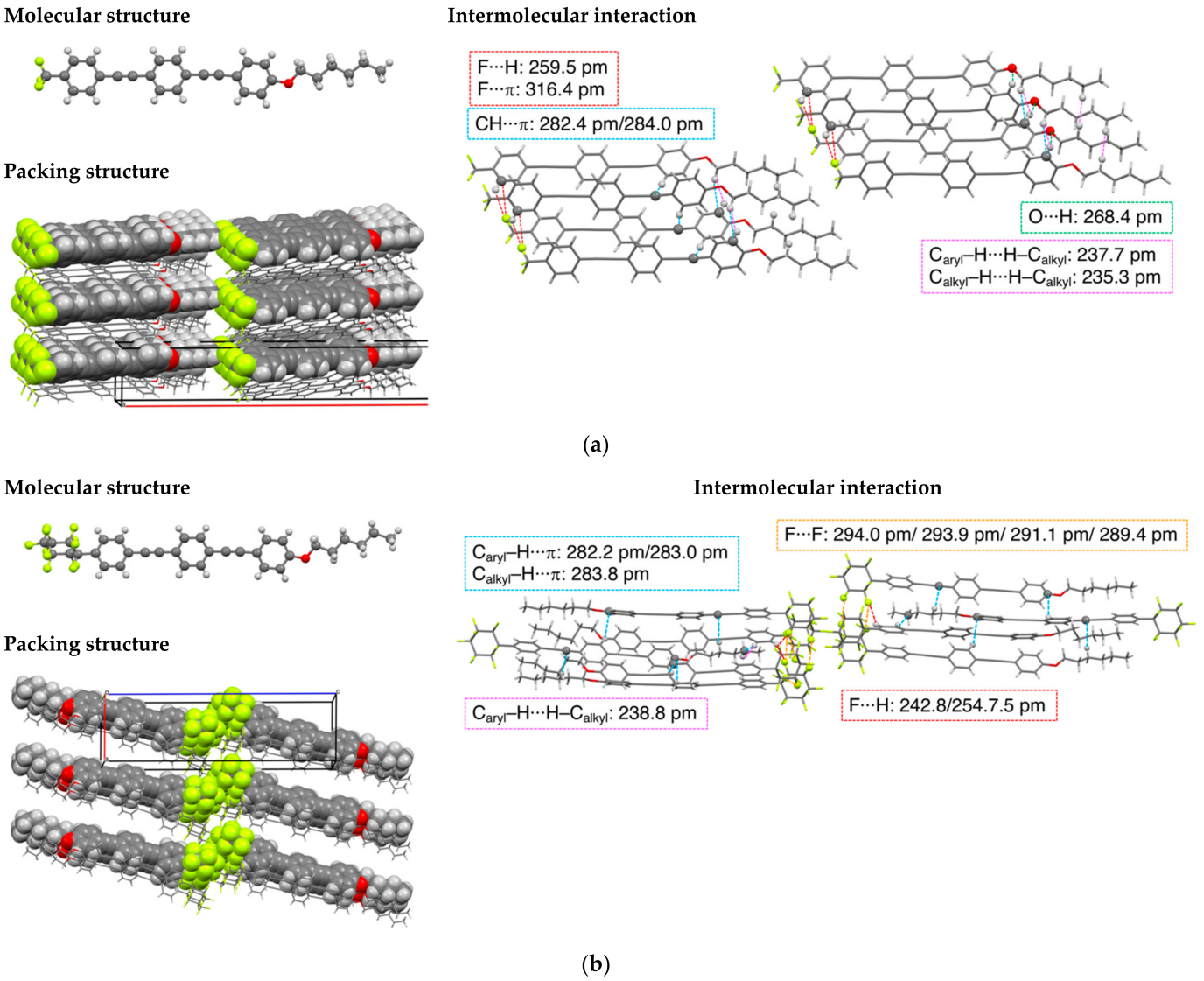


**Figure 4.** Crystal structures, packing structures, and intermolecular interactions between neighboring molecules for (**a**) **2a** and (**b**) **2c**.

### *3.3. Phase Transition Behaviors*

The phase transition behaviors of crystalline bistolane derivatives **1a** and **1b** and **2a**–**2c** were then evaluated using polarizing optical microscopy (POM), differential scanning calorimetry (DSC), and variable temperature powder X-ray diffraction (VT-PXRD). Figure 5 shows the phase sequences and POM images observed for the LC phase during the 2nd heating and cooling processes.

During the POM observations, a bright-viewing field with good fluidity was found for all the bistolanes (i.e., **1a**, **1b**, and **2a**–**2c**) over both the heating and cooling processes. The POM images of **1a** and **1b** in the LC phase display the four-brush Schlieren texture, which is a typical image of a nematic (N) LC phase. In addition, the VT-PXRD measurements of **1a** and **1b** at 180 °C revealed a hollow pattern at ~20° (2$\theta$) with no sharp diffraction signals. Based on the POM and VT-PXRD measurements, the observed LC phases for **1a** and **1b** were identified as the nematic (N) phase with an orientational order. In contrast to the alkyl-substituted **1a** and **1b**, $CF_3$-substituted **2a** and *cyclo*-$C_6F_{11}$-substituted **2c** displayed distinct POM textures, namely fan-shaped arrangements, which are typical textures for smectic (Sm) phases with both orientational order and positional order in the LC phase. In the case of **2a**, which bears a $CF_3$-unit, VT-PXRD measurements at 150° showed three sharp peaks, identified as the (110), (200), and (210) mirror indexes, in the wide-angle region.

This indicates that **2a** forms an in-plane herringbone structure (Figure S23, Supporting Information). Consequently, the LC phase observed between 130 and 202 °C was identified as a smectic E (SmE) phase [44]. Furthermore, the PXRD pattern at 210 °C showed only one sharp diffraction peak, assigned to the (110) plane, which corresponds to a hexagonal structure; the LC phase observed in the range of 202–214 °C was identified as the smectic B (SmB) phase. Additionally, the LC phase displayed between 214 and 236 °C was identified as the smectic A (SmA) phase, which produced a single sharp diffraction peak in the small-angle region. In contrast, for **2c,** which bears a *cyclo*-$C_6H_{11}$ unit, a single sharp signal was detected in the small-angle region at 180 °C, which indicates that **2c** displayed only the SmA phase in the LC form (Figure S25 in SI). Although **2b,** which bears an all-*cis*-2,3,5,6-tetrafluorocyclohexyl (*cis-cyclo*-$C_6H_7F_4$) unit, contained four fluorine atoms in its flexible unit, only the N phase was observed as an LC phase, analogous to the case of **1**, which bears an alkyl chain. Based on these observations, the dipole moment $\mu_{||}$ along the major molecular axis was considered to be important for controlling the LC phase. More specifically, the incorporation of fluorine atoms to increase $\mu_{||}$ induces the formation of a higher-order LC phase with both orientational and positional order, similar to the Sm phase, whereas bistolanes with smaller $\mu_{||}$ values form an LC phase with only an orientational order, such as the N phase.

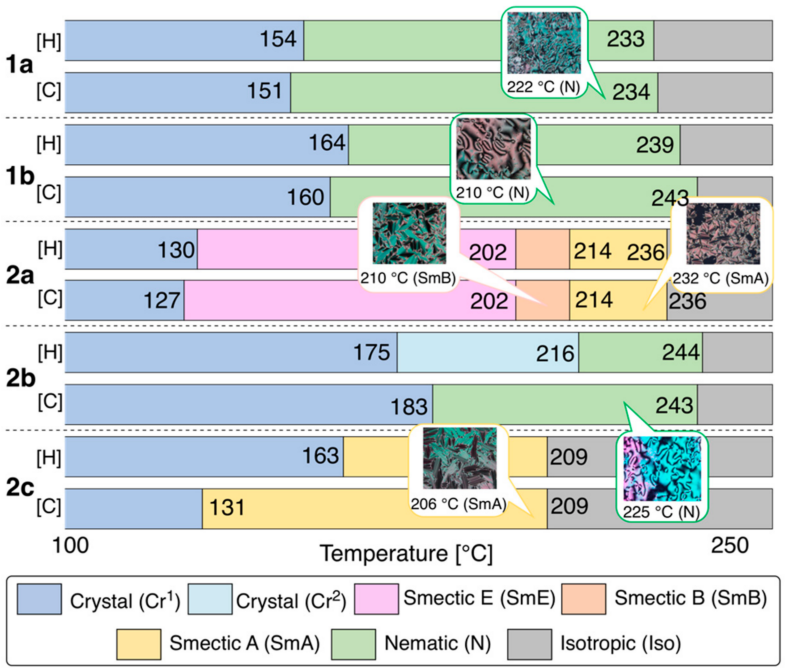


**Figure 5.** Phase transition behaviors of the bistolane derivatives during the 2nd heating [H] and cooling [C] processes (scan rate: 5.0 °C $min^{-1}$). POM texture images of the LC phases are also shown.

### *3.4. Photophysical Behavior*

Subsequently, we focused on the photophysical behaviors of bistolanes **1a** and **1b,** which bear an alkyl chain, and **2a**–**2c**, which bear a fluoroalkyl unit. Figure 6a shows the UV–Vis absorption ($1.5 \times 10^{-5}$ mol $L^{-1}$) and PL spectra ($1.0 \times 10^{-6}$ mol $L^{-1}$) in $CH_2Cl_2$, and the obtained photophysical data are summarized in Table 2.

For the UV–Vis absorption measurements carried out in $CH_2Cl_2$, a single UV–Vis absorption band ($\lambda_{abs}$) was observed for all bistolanes with a maximum absorption wavelength at ~328–332 nm, together with a shoulder peak at ~348–350 nm (Figure 6a, Table 2). Based on the theoretical assessment ($\lambda^{calcd}$ = 330–334 nm, Table 1), for all compounds, the major absorption band was concluded to originate from the HOMO→LUMO transition. The slight red-shift of the $\lambda_{abs}$ values of **2a**–**2c**, compared to those of **1a** and **1b**, were likely caused by the narrower HOMO–LUMO energy gap ($\Delta E$) of the former, which is induced by the electron-withdrawing character of the fluoroalkyl unit.

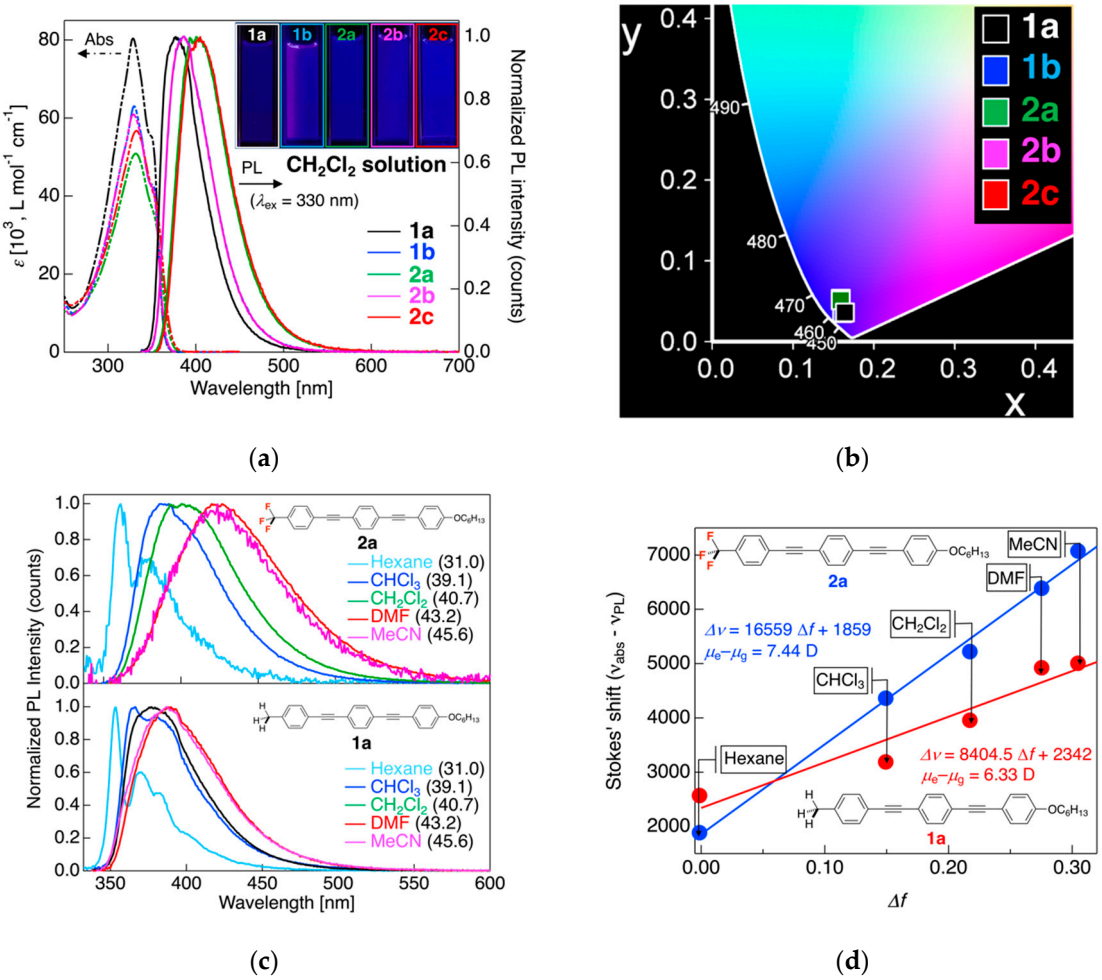


**Figure 6.** (**a**) UV–Vis and PL spectra of **1a**, **1b**, and **2a**–**2c** measured in $CH_2Cl_2$ (inset: photographic images of the PL observed under UV irradiation at $\lambda_{ex}$ = 365 nm); (**b**) Commission Internationale de l'Eclailage (CIE) diagram indicating the PL color; (**c**) PL spectra of **1a** and **2a** in various solvents. The values in parentheses indicate the $E_T(30)$ values, which are quantitative indicators of the solvent polarity; (**d**) Lippert–Mataga plot calculated from the Stokes' shift ($\Delta\nu = \nu_{abs} - \nu_{PL}$) and a solvent polarity parameter ($\Delta f$).

**Table 2.** Photophysical data for **1a**, **1b**, and **2a**–**2c** recorded in various solvents [1].

| Compound | Solvent [$E_T(30)$] [2] | $\lambda_{abs}$ (nm) [$\varepsilon$, $10^3$ L mol$^{-1}$ cm$^{-1}$] | $\lambda_{ex}$ (nm) | $\lambda_{PL}$ (nm) | $\Phi_{PL}$ [3] |
|---|---|---|---|---|---|
| **1a** | $CH_2Cl_2$ [40.7] | 328 [80.4], 348 [sh, 55.6] | 330 | 377 | 1.00 |
| | Hexane [31.0] | 324 [20.4], 344 [sh, 12.9] | 324 | 353, 368, 380 | 0.30 |
| | $CHCl_3$ [39.1] | 328 [57.2], 348 [sh, 37.3] | 330 | 366, 380 | 0.66 |
| | DMF [43.2] | 328 [33.7], 348 [sh, 23.2] | 330 | 388 | 0.78 |
| | MeCN [45.6] | 324 [38.1], 344 [sh, 26.8] | 324 | 388 | 0.68 |
| **1b** | $CH_2Cl_2$ [40.7] | 330 [63.0], 350 [sh, 43.0] | 330 | 386 | 1.00 |
| **2a** | $CH_2Cl_2$ [40.7] | 331 [50.9], 350 [sh, 37.0] | 330 | 400 | 1.00 |
| | Hexane [31.0] | 330 [2.6], 349 [sh, 1.4] | 330 | 361, 377 | 0.20 |
| | $CHCl_3$ [39.1] | 333 [23.4], 350 [sh, 19.0] | 330 | 388 | 0.86 |
| | DMF [43.2] | 333 [23.4], 350 [sh, 19.0] | 330 | 420 | 0.83 |
| | MeCN [45.6] | 325 [5.3], 346 [sh, 3.7] | 325 | 420 | 0.71 |
| **2b** | $CH_2Cl_2$ [40.7] | 329 [61.0], 350 [sh, 42.4] | 330 | 386 | 1.00 |
| **2c** | $CH_2Cl_2$ [40.7] | 332 [56.7], 350 [sh, 41.7] | 330 | 405 | 1.00 |

[1] Concentration: $1.0 \times 10^{-5}$ mol L$^{-1}$ for the UV–Vis absorption measurements and $1.0 \times 10^{-6}$ mol L$^{-1}$ for the PL measurements. [2] The $E_T(30)$ value is a quantitative indicator of the solvent polarity. [3] Measured using an integrating sphere; sh: shoulder peak.

Upon irradiation of the $CH_2Cl_2$ solutions of the bistolanes with UV light of an energy equal to $\lambda_{abs}$, all compounds were found to exhibit strong PL ($\Phi_{PL}$ = 1.00), with a single PL band of maximum PL wavelength ($\lambda_{PL}$) at ~377–405 nm (Figure 6a, Table 2). In this case, the incorporation of fluorine atoms into the flexible unit caused a gradual red-shift in $\lambda_{PL}$ by 20–23 nm for **2a** and **2c**, with respect to the values for **1a** and **1b**, although **2b**, which contained four fluorine atoms, did not exhibit any such shift in $\lambda_{PL}$. Using theoretical assessments, it was concluded that the red-shift in $\lambda_{PL}$ is associated with the orbital gap ($\Delta E$) between the HOMO and LUMO; full substitution of the flexible unit with fluorine atoms, as in the cases of **2a** and **2c**, caused a 0.12 eV decrease in $\Delta E$ compared to that of their non-fluorinated counterparts, i.e., **1a** and **1b**, resulting in a slight red-shift in $\lambda_{PL}$. However, the partial incorporation of fluorine atoms into the flexible unit, as in the case of **2b**, had no significant impact, and this was attributed to the less effective electron withdrawing capability of the flexible unit along the major molecular axis. As shown by the Commission Internationale de l'Eclailage (CIE) color diagram in Figure 6b, all the bistolane analogues produced a deep blue PL color in $CH_2Cl_2$.

To gain additional insight into the effect of fluorine atoms on the absorption and PL behaviors, the influence of the solvent was examined for $CH_3$-substituted **1a** and $CF_3$-substituted **2a** as a representative comparison (Figure 6c). It was found that the absorption behaviors of **1a** and **2a** were consistent, without showing any dependence on the solvent polarity, i.e., $\lambda_{abs}$ = 324–328 nm for **1a** and 325–333 nm for **2a** (Figures S28 and S29 in SI). By contrast, the PL behavior was found to change upon varying the solvent polarity. More specifically, a solution of **1a** in the less polar hexane ($E_T(30)$ = 31.0) [45] exhibited sharp PL signals at ~353 nm, along with a vibrational structure at ~368 nm. Upon increasing the solvent polarity, the PL band was gradually shifted to the long-wavelength region, reaching up to 388 nm when DMF ($E_T(30)$ = 43.2) or MeCN ($E_T(30)$ = 45.6) was employed as the solvent. $CF_3$-substituted **2a** also exhibited a sharp band at ~361 nm in hexane, together with vibrational structure at ~377 nm. In the case of **2a**, the $\lambda_{PL}$ reached up to 420 nm when the polar solvents DMF ($E_T(30)$ = 45.6) or MeCN ($E_T(30)$ = 45.6) were used. Upon comparison of the PL behaviors of **1a** and **2a** in various solvents, a longer-wavelength shift in the PL was observed in the case of $CF_3$-substituted **2a** because **2a** is likely to be susceptible to stabilization via solvation in polar solvents due to its large dipole moment, $\mu_{||}$. To elucidate the correlation between solvent polarity and PL behavior, Lippert–Mataga plots were created with a solvent polarity parameter ($\Delta f$) on the horizontal axis and the Stokes' shift ($\Delta\nu = \nu_{abs} - \nu_{PL}$) on the vertical axis (Figure 6d) [46,47]. Linear relationships between $\Delta\nu$ and $\Delta f$ were found for **1a** and **2a**, and these are expressed in Equations (1) and (2), respectively:

$$\Delta\nu = 8404.5\ \Delta f + 2342, \quad (1)$$

$$\Delta\nu = 16{,}559\ \Delta f + 1859, \quad (2)$$

It is known that the slope of these equations is strongly correlated with the difference in the dipole moments between the excited and ground states [44]: $\Delta\mu = \mu_e - \mu_g$, where $\mu_e$ and $\mu_g$ represent the dipole moments in the excited and ground states, respectively. As a result, the value of $\Delta\mu$ for **2a** was larger than that for **1a** (i.e., 7.44 D for **2a** and 6.33 D for **1a**), and this was attributed to the fact that compared to **1a**, the $CF_3$-substituted **2a** is likely to exhibit a larger polarization in the excited state. Therefore, the incorporation of a fluoroalkyl substituent resulted in a strong intermolecular charge transfer transition-based PL due to the strong electron-withdrawing character of the fluoroalkyl unit.

It is of significant interest that bistolanes **1a** and **1b** (bearing an alkyl chain) and **2a**–**2c** (bearing a fluoroalkyl unit) exhibited PL even in the crystalline state, despite the fact that the majority of $\pi$-conjugated luminophores have been reported to undergo immediate quenching when molecular aggregates are formed [48,49]. Figure 7 shows the PL spectra and photographic images depicting the PL behaviors of **1a**, **1b**, and **2a**–**2c** in the crystalline state, along with the corresponding CIE color diagram. The corresponding photophysical data are listed in Table 3.

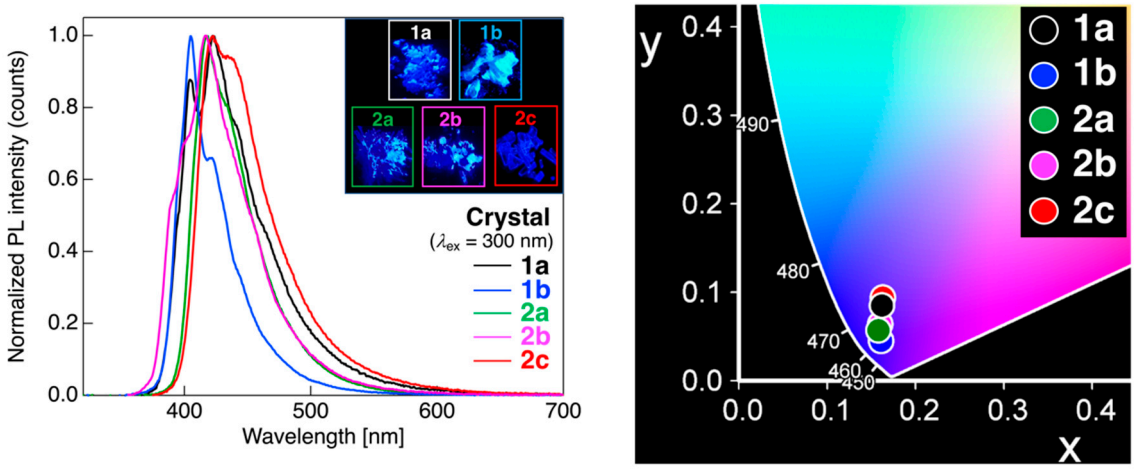


(**a**) (**b**)

**Figure 7.** (**a**) PL spectra of **1a**, **1b**, and **2a**–**2c** in the crystalline form (inset: photographic images showing PL under UV irradiation at $\lambda_{ex}$ = 365 nm); (**b**) CIE color diagram obtained from the corresponding PL spectra.

**Table 3.** Photophysical data for **1a**, **1b**, and **2a**–**2c** in the crystalline form.

| Compound | $\lambda_{PL}$ [1] | $\Phi_{PL}$ [2] |
|---|---|---|
| **1a** | 404, 422 | 0.57 |
| **1b** | 405, 421 | 0.79 |
| **2a** | 418, 434(sh) | 1.00 |
| **2b** | 401(sh), 417 | 0.71 |
| **2c** | 421, 434(sh) | 0.82 |

[1] Excitation wavelength of incident light: 300 nm; sh: shoulder peak. [2] Measured using an integrating sphere.

As indicated in Figure 7a, compounds **1a** and **1b** exhibited two PL bands with $\lambda_{PL}$ values of ~404 and 422 nm, while bands at ~418, 417, and 421 nm, were observed for **2a**–**2c**, respectively, in addition to shoulder peaks at 434 nm for **2a** and **2c**, and at 401 nm for **2b**. In comparison with the results obtained for the alkyl-containing **1a** and **1b**, the $\lambda_{PL}$ values for **2a**–**2c** were slightly red-shifted by 10–15 nm. In addition, $\lambda_{PL}$ was significantly red-shifted by ~30 nm, in comparison with the $\lambda_{PL}$ obtained in the solution states, which is attributable to the stabilization of the excited states via intermolecular interactions in the aggregated states.

It is noteworthy that bistolanes **1a** and **1b** exhibited high PL efficiencies ($\Phi_{PL}$) of 0.57 and 0.79, respectively, even in the crystalline state, although the values of $\Phi_{PL}$ in the aggregated states were drastically reduced compared with those in the solution states, due to the acceleration of non-radiative deactivation via intermolecular interactions [48,49]. As mentioned above, **2b**, which contains a partially fluorinated alkyl unit, afforded a similar result for the PL measurements, even in the crystalline state, whereas bistolanes **2a** and **2c**, which bear fully fluorinated alkyl units, exhibited enhanced $\Phi_{PL}$ values. As discussed above, **2a** and **2c** formed rigid molecular aggregates through multiple intermolecular interactions, which effectively weakened the molecular motions (e.g., vibration and rotation). This, in turn, suppressed non-radiative deactivation, and produced a significant enhancement in $\Phi_{PL}$. In the other compounds, it is anticipated that non-radiative deactivation cannot be sufficiently suppressed because there are fewer intermolecular interactions, although the aggregated structures of non-fluorinated **1a** and **1b** and partially fluorinated **2b** remain unclear. Accordingly, the incorporation of a fluoroalkyl unit into the bistolane scaffold can achieve rigid packing in the molecular aggregates, leading to a significant enhancement in the $\Phi_{PL}$, even in the crystalline state.

Notably, the bistolane derivatives bearing a non-fluorinated or fluorinated alkyl chain were also found to be emissive in their LC phase that was formed after a thermal transition from the crystalline to the LC phase. The PL intensity, however, was gradually retarded

because of the increasing non-radiative deactivation via micro-Brownian motion under the thermal conditions. The photoluminescent liquid crystal (PLLC) characteristics could be significantly improved if alignment of the LC on a film or substance could be controlled using a photoalignment technique, such as a mechanical rubbing process [50] or a rubbing-free process using photo-cross-linkable polymers [51,52] and photoreactive polyimide polymers [53,54].

## 4. Conclusions

To elucidate the effects of fluorine atoms in bistolane-based photoluminescent liquid crystals (PLLCs) on their liquid-crystalline (LC) and photoluminescent (PL) behaviors, bistolanes bearing an alkyl chain or a fluoroalkyl unit were synthesized, and their physical behaviors were systematically evaluated. All bistolanes exhibited LC behavior; the non-fluorinated alkyl-containing bistolanes mainly displayed a nematic LC phase, whereas their fluoroalkyl-containing counterparts exhibited smectic LC phases that possessed both an orientational order and a positional order. The large difference in the LC behavior can be attributed to two factors, namely the dipole moment along a major molecular axis, which is induced by the electron-withdrawing fluoroalkyl units, and the construction of head-to-tail or head-to-head ordered structures in molecular aggregates through F···H or F···F intermolecular interactions. In the photophysical measurements, interestingly, all bistolanes exhibited an intense PL behavior both in the dilute solution and in the crystalline phases. The incorporation of fluorine atoms into the flexible unit reduced not only the HOMO and LUMO energy levels, but also the energy gap between the two, thereby generating a slight red-shift of the maximum PL wavelength. Although the PL efficiency in the crystalline state normally decreases via non-radiative deactivation induced by intermolecular energy transfer, it was notable that the bistolanes containing fluoroalkyl units exhibited enhanced PL efficiencies due to the effective suppression of non-radiative deactivation. This was attributed to the formation of rigid molecular packing structures through multiple intermolecular interactions involving F···H and F···F interactions, among others. Consequently, the incorporation of fluorine atoms into the flexible units of the bistolane-based PLLCs likely contributed to the generation of a higher-ordered smectic LC phase in addition to blue PL in both the solution and aggregated states, with a high PL efficiency. These results will pave the way for the development of high-performance functional materials by incorporating fluorine atoms into organic molecules. Further fluorine-containing PLLCs will be reported by our research group in the near future.

**Supplementary Materials:** The following are available online at https://www.mdpi.com/article/10.3390/cryst11040450/s1, Figures S1–S13: NMR spectra, Figures S14 and S15: Crystal structure, Figures S16–S20: Optimized structures and their HOMO and LUMO distributions, Figures S21–25: DSC thermograms, Figure S26: POM image, Figures S27–S29: UV–Vis and PL spectra, Figure S30: Lippert–Mataga plots, Figure S31: Excitation and PL spectra, Table S1: Crystallographic data, Tables S2–S11: Cartesian coordinates for calculated structure, Tables S12–S16: phase transition behavior, Tables S17 and S18: photophysical data in a different solvent.

**Author Contributions:** Conceptualization, S.Y.; methodology, S.Y.; validation, S.Y. and M.M.; investigation, S.Y., M.M., Y.W., T.K. (Tsutomu Konno), Q.Z., D.O., M.N., T.A., H.F., T.K. (Toshio Kubota), and M.H.; resources, S.Y., M.M., Y.W., Q.Z., D.O.; data curation, S.Y., M.M., Y.W., T.K. (Tsutomu Konno); writing—original draft preparation, S.Y.; writing—review and editing, S.Y., M.M., Y.W., T.K. (Tsutomu Konno), Q.Z., D.O., M.N., T.A., H.F., T.K. (Toshio Kubota), and M.H.; visualization, S.Y.; supervision, S.Y.; project administration, S.Y.; funding acquisition, S.Y. All authors have read and agreed to the published version of the manuscript.

**Funding:** This research was funded by JSPS KAKENHI through a Grant-in-Aid for Scientific Research (C), grant number JP18K05262.

**Data Availability Statement:** Data is contained within the article and supplementary material.

**Conflicts of Interest:** The authors declare no conflict of interest.

## References


1. Caron, S. Where does the fluorine come from? A review on the challenges associated with the synthesis of organofluorine compounds. *Org. Process Res. Dev.* **2020**, *24*, 470–480. [CrossRef]
2. Inoue, M.; Sumii, Y.; Shibata, N. Contribution of organofluorine compounds to pharmaceuticals. *ACS Omega* **2020**, *5*, 10633–10640. [CrossRef] [PubMed]
3. Ogawa, Y.; Tokunaga, E.; Kobayashi, O.; Hirai, K.; Shibata, N. Current contributions of organofluorine compounds to the agrochemical industry. *iScience* **2020**, *23*, 101467. [CrossRef] [PubMed]
4. Kirsch, P. *Modern Fluoroorganic Chemistry: Synthesis, Reactivity, Applications*, 2nd ed.; Wiley-VCH: Weinheim, Germany, 2013; pp. 7–21.
5. Behrang, N.; Fischbach, F.; Kipp, M. Mechanism of siponimod: Anti-inflammatory and neuroprotective mode of action. *Cells* **2019**, *8*, 24. [CrossRef]
6. Mei, H.; Han, J.; Fustero, S.; Medio-Simon, M.; Sedgwick, D.M.; Santi, C.; Ruzziconi, R.; Soloshonok, V.A. Fluorine-containing drugs approved by the FDA in 2018. *Chem. Eur. J.* **2019**, *25*, 11797–11819. [CrossRef]
7. Böhm, H.-J.; Banner, D.; Bendels, S.; Kansy, M.; Kuhn, B.; Müller, K.; Obst-Sander, U.; Stahl, M. Fluorine in medicinal chemistry. *ChemBioChem* **2004**, *5*, 637–643. [CrossRef]
8. Lowe, P.T.; O'Hagan, D. A role for fluorine in flavours, fragrances and pheromones. *J. Fluor. Chem.* **2020**, *230*, 109420. [CrossRef]
9. Li, H.; Gao, M.; Chen, Y.; Wang, Y.; Zhu, X.; Yang, G. Discovery of pyrazine-carboxamide-diphenyl-ethers as novel succinate dehydrogenase inhibitors via fragment recombination. *J. Agric. Food Chem.* **2020**, *68*, 14001–14008. [CrossRef]
10. Giornal, F.; Pazenok, S.; Rodefeld, L.; Lui, N.; Vors, J.-P.; Leroux, F.R. Synthesis of diversely fluorinated pyrazoles as novel active agrochemical ingredients. *J. Fluor. Chem.* **2013**, *152*, 2–11. [CrossRef]
11. Fan, Q.; Méndez-Romero, U.; Guo, X.; Wang, E.; Zhang, M.; Li, Y. Fluorinated photovoltaic materials for high-performance organic solar cells. *Chem. Asian J.* **2019**, *14*, 3085–3095. [CrossRef]
12. Funabiki, K.; Saito, Y.; Kikuchi, T.; Yagi, K.; Kubota, Y.; Inuzuka, T.; Miwa, Y.; Yoshida, M.; Sakurada, O.; Kutsumizu, S.J. Aromatic Fluorine-Induced One-Pot Synthesis of Ring-Perfluorinated Trimethine Cyanine Dye and Its Remarkable Fluorescence Properties. *J. Org. Chem.* **2019**, *84*, 4372–4380. [CrossRef]
13. Hird, M. Fluorinated liquid crystals—Properties and applications. *Chem. Soc. Rev.* **2007**, *36*, 2070–2095. [CrossRef]
14. Konno, T. Trifluoromethylated internal alkynes: Versatile building blocks for the preparation of various fluorine-containing molecules. *Synlett* **2014**, *25*, 1350–1370. [CrossRef]
15. Konno, T. Trifluoromethyl ($CF_3$) group insertion methods in stereoselective synthesis. In *Stereoselective Synthesis of Drugs and Natural Products*; Andrunshko, V., Andrunshko, N., Eds.; John Wiley & Sons: Hoboken, NJ, USA, 2013; pp. 769–806.
16. Yamada, S.; Konno, T. New types of negative dielectric anisotropy liquid crystals: Synthesis of $CF_2CF_2$-carbocyclic mesogens and an evaluation of their liquid crystal characteristics. In *Chemical Elements (Fluorine, Rhodium and Rubidium): Properties, Synthesis and Applications*; Huff, A., Ed.; Nova Science Publishers: New York, NY, USA, 2018; pp. 53–92.
17. Yamada, S.; Mitsuda, A.; Miyano, K.; Tanaka, T.; Morita, M.; Agou, T.; Kubota, T.; Konno, T. Development of novel solid-state light-emitting materials based on pentafluorinated tolane fluorophores. *ACS Omega* **2018**, *3*, 9105–9113. [CrossRef]
18. Morita, M.; Yamada, S.; Konno, T. Fluorine-induced emission enhancement of tolanes via formation of tight molecular aggregates. *New J. Chem.* **2020**, *44*, 6704–6708. [CrossRef]
19. Yamada, S.; Mitsuda, A.; Adachi, K.; Hara, M.; Konno, T. Development of light-emitting liquid-crystalline polymers with a pentafluorinated bistolane-based luminophore. *New J. Chem.* **2020**, *44*, 5684–5691. [CrossRef]
20. Morita, M.; Yamada, S.; Agou, T.; Kubota, T.; Konno, T. Luminescence tuning of fluorinated bistolanes via electronic or aggregated-structure control. *Appl. Sci.* **2019**, *9*, 1905. [CrossRef]
21. Yamada, S.; Morita, M.; Agou, T.; Kubota, T.; Ichikawa, T.; Konno, T. Thermoresponsive luminescence properties of polyfluorinated bistolane-type light-emitting liquid crystals. *Org. Biomol. Chem.* **2018**, *16*, 5609–5617. [CrossRef]
22. Yamada, S.; Morita, M.; Konno, T. Multi-color photoluminescence induced by electron-density distribution of fluorinated bistolane derivatives. *J. Fluorine Chem.* **2017**, *202*, 54–64. [CrossRef]
23. Yamada, S.; Miyano, K.; Konno, T.; Agou, T.; Kubota, T.; Hosokai, T. Fluorine-containing bistolanes as light-emitting liquid crystalline molecules. *Org. Biomol. Chem.* **2017**, *15*, 5949–5958. [CrossRef]
24. Nishikawa, M.; Kume, S.; Nishihara, H. Stimuli-responsive pyrimidine ring rotation in copper complexes for switching their physical properties. *Phys. Chem. Chem. Phys.* **2013**, *15*, 10549–10565. [CrossRef]
25. Kobayashi, A.; Kato, M. Stimuli-responsive luminescent copper(I) complexes for intelligent emissive devices. *Chem. Lett.* **2017**, *46*, 154–162. [CrossRef]
26. Sheldrick, G.M. Crystal structure refinement with SHELEX. *Acta Cryst.* **2015**, *C71*, 3–8.
27. Frisch, M.J.; Trucks, G.W.; Schlegel, H.B.; Scuseria, G.E.; Robb, M.A.; Cheeseman, J.R.; Scalmani, G.; Barone, V.; Petersson, G.A.; Nakatsuji, H.; et al. *Gaussian 16, Revision B.01*; Gaussian, Inc.: Wallingford, CT, USA, 2016.
28. Zhao, Y.; Truhlar, D.G. The M06 suite of density functionals for main group thermochemistry, thermochemical kinetics, noncovalent interactions, excited states, and transition elements: Two new functionals and systematic testing of four M06-class functionals and 12 other functionals. *Theor. Chem. Acc.* **2008**, *120*, 215–241.
29. Chan, B.; Gilbert, A.T.B.; Gill, P.M.W.; Radom, L. Performance of density functional theory procedures for the calculation of proton-exchange barriers: Unusual behavior of M06-type functionals. *J. Chem. Theory Comput.* **2014**, *10*, 3777–3783. [CrossRef]

30. Andzelm, J.; Kölmel, C.; Klamt, A. Incorporation of solvent effects into density functional calculations of molecular energies and geometries. *J. Chem. Phys.* **1995**, *103*, 9312–9320. [CrossRef]
31. Barone, V.; Cossi, M. Quantum calculation of molecular energies and energy gradients in solution by a conductor solvent model. *J. Phys. Chem. A* **1998**, *102*, 1995–2001. [CrossRef]
32. Cossi, M.; Rega, N.; Scalmani, G.; Barone, V. Energies, structures, and electronic properties of molecules in solution with the C-PCM solvation model. *J. Comput. Chem.* **2003**, *24*, 669–681. [CrossRef]
33. Grad, J.; Yan, Y.J.; Mukamel, S. Time-dependent self-consistent field approximation for semiclassical dynamics using Gaussian wavepackets in phase space. *Chem. Phys. Lett.* **1987**, *134*, 291–295. [CrossRef]
34. Makri, N. Time-dependent self-consistent field approximation with explicit two-body correlations. *Chem. Phys. Lett.* **1990**, *169*, 541–548. [CrossRef]
35. Durie, A.J.; Slawin, A.M.Z.; Lebl, T.; Kirsch, P.; O'Hagan, D. Fluorocyclohexenes: Synthesis and structure of all-syn-1,2,4,5-tetrafluorocyclohexane. *Chem. Commun.* **2012**, *48*, 9643–9645. [CrossRef] [PubMed]
36. Durie, A.J.; Fujiwara, T.; Cormanich, R.; Bühl, M.; Slawin, A.M.Z.; O'Hagan, D. Synthesis and elaboration of all-cis-1,2,4,5-tetrafluoro-3-phenylcyclohexane: A polar cyclohexane motif. *Chem. Eur. J.* **2014**, *20*, 6259–6263. [CrossRef] [PubMed]
37. Kawahara, S.; Tsutzuki, S.; Uchimaru, T. Theoretical study of the C–F/$\pi$ interaction: Attractive interaction between fluorinated alkane and an electron-deficient $\pi$-system. *J. Phys. Chem. A* **2004**, *108*, 6744–6749. [CrossRef]
38. Li, P.; Maier, J.M.; Vik, E.C.; Yehl, C.J.; Dial, B.E.; Rickher, A.E.; Smith, M.D.; Pellechia, P.J.; Shimizu, K.D. Stabilizing fluorine–$\pi$ interactions. *Angew. Chem. Int. Ed.* **2017**, *56*, 7209–7212. [CrossRef]
39. Mooibroek, T.J.; Gamez, P.; Reedijk, J. Lone pair–$\pi$ interactions: A new supramolecular bond? *CrystEngComm* **2008**, *10*, 1501–1515. [CrossRef]
40. Bondi, A. van der Waals volumes and radii. *J. Phys. Chem.* **1964**, *68*, 441–451. [CrossRef]
41. Bauzá, A.; Frontera, A. Electrostatically enhanced F···F interactions through hydrogen bonding, halogen bonding and metal coordination: An ab initio study. *Phys. Chem. Chem. Phys.* **2016**, *18*, 20381–20388. [CrossRef]
42. Beker, R.J.; Colavita, P.E.; Murphy, D.M.; Platts, J.A.; Wallis, J.D. Fluorine-fluorine interactions in the solid state: An experimental and theoretical study. *J. Phys. Chem. A* **2012**, *116*, 1435–1444. [CrossRef]
43. Takezawa, H.; Murase, T.; Resnati, G.; Metrangolo, P.; Fujita, M. Recognition of polyfluorinated compounds through self-aggregation in a cavity. *J. Am. Chem. Soc.* **2014**, *136*, 1786–1788. [CrossRef]
44. Sugisawa, S.; Tabe, Y. Induced smectic phases of stoichiometric liquid crystal mixtures. *Soft Matter.* **2016**, *12*, 3103–3109. [CrossRef]
45. Reichardt, C. Solvatochromic dyes as solvent polarity indicators. *Chem. Rev.* **1994**, *94*, 2319–2358. [CrossRef]
46. Mataga, N.; Kaifu, Y.; Koizumi, M. The solvent effect on fluorescence spectrum, change of solute-solvent interaction during the lifetime of excited solute molecule. *Bull. Chem. Soc. Jpn.* **1955**, *28*, 690–691. [CrossRef]
47. Mataga, N.; Kaifu, Y.; Koizumi, M. Solvent effects upon fluorescence spectra and the dipole moments of excited molecules. *Bull. Chem. Soc. Jpn.* **1956**, *29*, 465–470. [CrossRef]
48. Birks, J.B. *Photophysics of Aromatic Molecules*; Birks, J.B., Ed.; Wiley: London, UK, 1970.
49. Thomas, S.W.; Joly, G.D.; Swager, T.M. Chemical sensors based on amplifying fluorescent conjugated polymer. *Chem. Rev.* **2007**, *107*, 1339–1386. [CrossRef]
50. Yaroshchuk, O.; Reznikov, Y. Photoalignment of liquid crystals: Basics and current trends. *J. Mater. Chem.* **2012**, *22*, 286–300. [CrossRef]
51. Kawatsuki, N.; Goto, K.; Yamamoto, T. Photoinduced anisotropy and photoalignment of nematic liquid crystals by a novel polymer liqud crystal with a coumarin-containing side group. *Liq. Cryst.* **2001**, *28*, 1171–1176. [CrossRef]
52. Kawatsuki, N.; Kuwabara, M.; Matsuura, Y.; Sasaki, T.; Ono, H. Photoalignment control of liquid crystals on photo-cross-linkable polymer liquid crystal film. *J. Photopolym. Sci. Technol.* **2005**, *18*, 17–22.
53. Li, X.D.; Zhong, Z.X.; Lee, S.H.; Ghang, G.; Lee, M.H. Liquid crystal photoalignment using soluble photosensitive polyimide. *Jpn. J. Appl. Phys.* **2006**, *45*, 906. [CrossRef]
54. Zhong, Z.X.; Li, X.; Lee, S.H.; Lee, M.H. Liquid crystal photoalignment material based on chloromethylated polyimide. *Appl. Phys. Lett.* **2004**, *85*, 2520. [CrossRef]